Spatially and temporally resolved measurements of NO_x fluxes by airborne eddy-covariance over Greater London

Adam R. Vaughan[1], James D. Lee[1,2], Stefan Metzger[3,4], David Durden[3], Alastair C. Lewis[1,2], Marvin D. Shaw[1,2], Will S. Drysdale[1,2], Ruth M. Purvis[1,2], Brian Davison[5] and C. Nicholas Hewitt[5]

[1]Wolfson Atmospheric Chemistry Laboratories, Department of Chemistry, University of York, York, YO10 5DD, UK
[2]National Centre for Atmospheric Science, University of York, York, YO10 5DD, UK
[3]National Ecological Observatory Network Program, Battelle, 1685 38th Street, Boulder, CO 80301, USA
[4]Department of Atmospheric and Oceanic Sciences, University of Wisconsin-Madison, 1225 West Dayton Street, Madison, WI 53706, USA
[5]Lancaster Environment Centre, Lancaster University, Lancaster, UK

Correspondence to: Adam R. Vaughan (adam.vaughan@york.ac.uk)

Abstract.

Flux measurements of nitrogen oxides (NO_x) were made over London using airborne eddy-covariance from a low flying aircraft. Seven low altitude flights were conducted over Greater London performing multiple over-passes across the city during eight days in July 2014. NO_x fluxes across the Greater London region (GLR) exhibited high heterogeneity and strong diurnal variability, with central areas responsible for the highest emission rates (20 - 30 mg m^{-2} h^{-1}). Other high emission areas included the M25 orbital motorway. The complexity of London's emission characteristics makes it challenging to pinpoint single emission sources definitively using airborne measurements. Multiple sources, including road transport and residential, commercial and industrial combustion sources are all likely to contribute to measured fluxes. Measured flux estimates were compared to scaled National Atmospheric Emissions Inventory (NAEI) estimates, accounting for; monthly, daily and hourly variability. Significant differences were found between the flux-driven emissions and the NAEI estimates across Greater London, with measured values up to two times higher in Central London than those predicted by the inventory. To overcome the limitations of using the national inventory to contextualise measured fluxes, we used physics-guided flux data fusion to train environmental response functions (ERF) between measured flux and environmental drivers (meteorological and surface). The aim was to generate time-of-day emission surfaces using calculated ERF relationships for the entire GLR. 98% spatial coverage was achieved across GLR at 400 m^2 spatial resolution. All flight leg projections showed substantial heterogeneity across the domain, with high emissions emanating from Central London and major road infrastructure. The diurnal emission structure of the GLR was also investigated, through ERF, with the morning rush-hour distinguished from lower emissions during the early afternoon. Overall, the integration of airborne fluxes with an ERF-driven strategy enabled the first independent generation of surface NO_x emissions, at high resolution using an eddy-covariance approach, for an entire city region.

Deleted: Greater London region (

Deleted:)

1 Introduction

Anthropogenic emissions of NO_x ($NO + NO_2 = NO_x$) occur over large areas of Europe and the United Kingdom, with atmospheric concentrations in many urban areas exceeding the recommended World Health Organisation (WHO) 40 µg m^{-3} annual health limit value (Brookes et al., 2013). Of all the common gaseous air pollutants, nitrogen dioxide (NO_2) is particularly problematic as it promotes respiratory diseases, such as lung inflammation, bronchial reactivity and a significant reduction in lung capacity (Foster et al., 2000; Kelly and Fussell, 2017; Shao et al., 2019). NO_2 also plays a central role in the production of ground-level ozone at the regional scale. London has operated a low emission zone (LEZ) since 2008, with the aim of reducing air pollution through vehicle-specific restrictions. The effectiveness of the current LEZ on respiratory health is still unclear, with some studies highlighting the need further to reduce NO_2 concentrations, before improvements in public health are achieved (Mudway et al., 2019). Analysis of UK and European road-side NO_x annual trends have shown a downward trend in NO_2 concentrations, however; road-side concentrations in regions such as Greater London remain well above WHO guidelines as of 2020 (Grange et al., 2017; Lang et al., 2019).

In order to bring atmospheric concentrations of air pollutants into alignment with air quality standards, it is first necessary to understand where the pollutant originates from so that effective legislative controls can be introduced. The National Atmospheric Emissions Inventory (NAEI) is the primary tool used by the UK Government for this purpose. A growing body of work has been conducted to evaluate the NAEI, by comparing inventory estimates with real-time flux measurements from towers and airborne platforms (Björkegren and Grimmond, 2018; Famulari et al., 2010; Font et al., 2015; Langford et al., 2009, 2010; Lee et al., 2015; Pitt et al., 2019; Vaughan et al., 2016, 2017).

Inventory validation is a vital component towards reducing urban pollutant concentrations, requiring a continued understanding of significant emission sources and spatial distributions. Eddy-covariance (EC) is a well-documented technique for quantifying atmospheric emission rates within the atmospheric boundary layer (Aubinet et al., 2012). Initially, EC studies focused on greenhouse gas emission assessment (Baldocchi, 2003), but these have now been extended to include reactive atmospheric compounds such as volatile organic carbon compounds (VOCs) and NO_x (Baldocchi, 2003; Karl et al., 2001, 2017, 2002; Langford et al., 2009, 2010; Lee et al., 2015; Marr et al., 2013; Squires et al., 2020; Vaughan et al., 2016).

The number of studies assessing NO_x emissions in urban environments is small and have focused mainly on point source analysis and emission inventory validation, highlighting often significant underestimation of emissions by inventories (Karl et al., 2017; Lee et al., 2015; Squires et al., 2020; Vaughan et al., 2016). The next stage in understanding complex urban emission topographies is to directly employ measured fluxes to calculate independent emissions grids. Here we present a new methodology for calculating high spatial resolution NO_x fluxes by airborne eddy-covariance and use these with other

Deleted: Here we present a new methodology for calculating high spatial resolution NO_x fluxes by airborne eddy-covariance and use these with other techniques to generate real-time emission grids over complex urban terrain. The method is demonstrated for the Greater London region but will be applicable to other metropolitan areas worldwide.…

Deleted: assessment

Deleted: employ

Deleted: be used tointerrogate of interest

techniques to generate real-time emission grids over complex urban terrain. The method is demonstrated for the GLR but will be applicable to other metropolitan areas worldwide.

2 Methods

2.1 Measurement campaign

Airborne eddy-covariance measurements were made during seven research flights as part of the Ozone Precurers Fluxes in an Urban Environment (OPFUE) project in July 2014 (Shaw et al., 2015; Vaughan et al., 2016, 2017). The project involved multiple low altitude flights over the GLR using the Natural Environment Research Council's (NERC) Dornier-228 aircraft, based at Gloucestershire Airport's Airborne Research and Survey Facility (ARSF). The aircraft has a maximum flight range of 2,600 km, science ceiling altitude of 4,500 m and a typical science flight speed of 74.5 ± 10 m s^{-1}.

Each research flight consisted of the following structure. An initial profile to 2,600 m was carried out at the beginning of each flight, allowing for calibrations in lower-NO_x air during the transit towards London. After transitting, a spiral descent over Goodwood (SE England), gave an estimation of boundary layer height. Straight level transects at 300-400 m were then flown across Greater London, starting at the southwest corner of the M25 orbital motorway and finishing at the opposite northeast edge of the GLR. A sharp right turn was then made towards the industrial areas of east London and over the Dartford Thames river crossing. The final transect ran perpendicular to the original, ending at the northwest corner of London, completing an open figure-of-eight design. The loop was not completed around the West of London, due to Heathrow airport. Each flight contained three repeat passes. Fig. 1 shows the flight path, with each transect type labelled. Table 1 summaries each transect type, the typical flight distance, location and the number of completed replicates. Only data collected during flights 3-7 will be presented due to instrument issues during flights 1-2.

Deleted: Greater London Region (

Deleted:)

Deleted: and science ceiling altitude of 4,500 m.

Deleted:

Transects	Length (km)	Start	Finish	Area Type	Replicates
1	50	51.30° N, 0.45° W	51.60° N, 0.18° E	suburban & urban	14
2	30	51.40° N, 0.20° E	51.62° N, 0.25° E	suburban & urban	5
3	30	51.40° N, 0.20° E	51.65° N, 0.15° E	suburban & urban	10
4	13	51.60° N, 0.10° E	51.50° N, 0.30° E	urban (major roads)	13
5	14	51.50° N, 0.30° E	51.40° N, 0.20° E	urban (major roads & industry)	16

Flight No.	Overpasses	Altitude (m)	Date	Duration	Weekday
3	2	329 ± 59	2014-07-12	13:00 – 15:00	Saturday
4	4	336 ± 55	2014-07-14	13:00 – 16:00	Monday
5	4	344 ± 31	2014-07-15	09:00 – 12:00	Tuesday
6	3	342 ± 78	2014-07-16	07:00 – 09:00	Wednesday
7	3	359 ± 89	2014-07-16	12:00 – 14:00	Wednesday

Table 1. Top) Individual flight transect information. Bottom) Flight information outlining; the time each flight occurred, the number of complete London overpasses and the altitude range.

Deleted: t
Deleted: / m
Deleted: s
Deleted: f
Deleted: a
Deleted: t
Deleted: r
Deleted: km
Deleted: km
Deleted: km
Deleted: km
Deleted: km
Deleted: and
Deleted: .
Deleted: Transect information

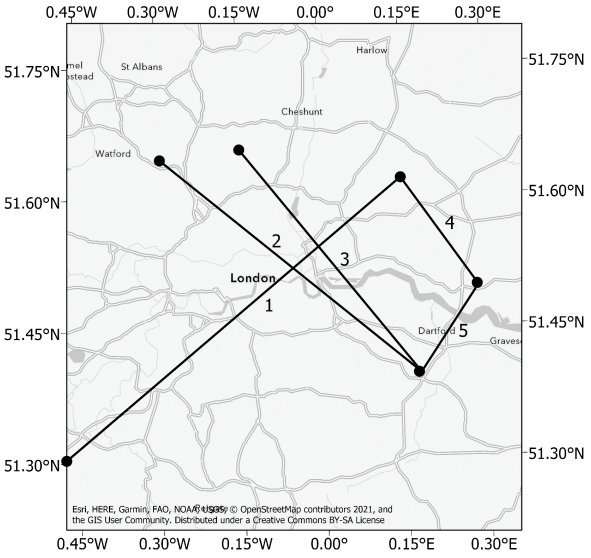

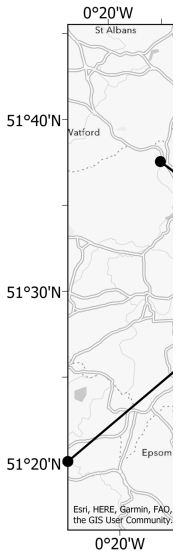

Deleted:

Figure 1. OPFUE 2014 flight path over Greater London, highlighting the incomplete figure of eight structure. Each transect type has been labelled. Plotted in ArcGIS® (Esri, 2021a).

2.2 Instrumentation

Eddy-covariance flux measurements of NO_x were made using an Air Quality Design Inc. (Golden, Colorado, USA) NO_x chemiluminescence analyser (Fast-AQD-NO_x). The instrument has a dual-channel architecture capable of quantifying ambient mixing ratios of NO and NO_2 sequentially (Squires et al., 2020). NO is quantified by the ozone-chemiluminescence reaction and NO_2 via the same detection method with an additional conversion of NO_2 to NO first (Drummond et al., 1985; Kley and McFarland, 1980; Lee et al., 2009; Reed et al., 2016). Ambient NO_2 is first photolytically converted to NO using a blue-light converter. After conversion, detection is achieved using the same ozone-chemiluminescence reaction as NO. Chemiluminescence detection is achieved using dry-ice cooled (-60 °C) photomultiplier tubes (PMTs) (Hamamatsu Photonics K. K.) with a red-window filter. As the resonance time within the NO_2 converter was found to be 0.11 s, NO and NO_2 mixing ratios were measured at a 9 Hz acquisition rate.

Deleted: at 9 Hz

Deleted: on

Deleted: Fig. 2 depicts the flow schematic for the instrument, showing two separate detection channels for NO and NO_2. Sample inlet pressure is kept at 266 hPa to negate the effect of changing altitude on instrument sensitivity. NO is quantified by the ozone-chemiluminescence reaction, with 100 sccm of O_3 added to a 1500 sccm sample flow

Deleted: Due to a

Deleted: 0.11 s

Deleted: of

Instrument precision was quantified by assessing the dark count noise on each PMT through frequency instrument zeros (supplementary, section 1.1) or by sampling NO_x free-air (Lee et al., 2009). Photon counting is a well-established technique, with rates following a Poisson distribution (Ingle and Crouch, 1972; Williamson et al., 1988). Instrument zeros were performed every 5 minutes during flight, except over the GLR, where zeros were performed during turns only. Fig. S2 shows for each flight the dark count distribution as a density area and the calculated Gaussian distribution. A Gaussian distribution was used over a Poisson, as the count rate (>3,000 counts s^{-1}) was high enough to ensure both distributions become identical (Lee et al., 2009; Silvia and Skilling, 2006). Across the campaign, the average 2σ precision using in-flight zeroes was calculated to be 153 and 249 pptv for NO and NO_2.

Instrument accuracy was assessed for systematic uncertainties. Sources of instrument inaccuracy were mass-flow controllers, calibration standards, the blue-light converter and channel artefacts. Instrument mass-flow controllers are accurate to ± 1% (manufacturer quoted). The NO/N_2 calibration standard has a quoted accuracy of ± 1% (supplied by BOC Group plc). The blue-light converter gives consistent, stable calibrations with an accuracy of ± 10% derived from signal stability of the CE calculation. By taking the individual uncertainties and propagating them, the overall uncertainty was calculated. Total uncertainty for a 1 ppb measurement of NO and NO_2 is 142.3% and 143.9% (at 9 Hz acquisition rate).

In addition to the Fast-AQD-NO_x, on-board instrumentation also included a Proton-Transfer-Reaction Mass-Spectrometer (PTR-MS; Ionicon GmbH), an Inertial-Position and Altitude System (IPAS 20) and an Aircraft Integrated Meteorological Measurement System (AIMMS-20; Aventech Research Inc.). The AIMMS-20 system delivers 20 Hz measurements of u,v,w wind vectors, temperature, pressure and relative humidity. The probe consists of five pitot-static pressure ports, configured in a cruciform array, giving horizontal and vertical wind speed measurements. The temperature and humidity sensors are located at the back of the probe in a reverse-flow housing to reduce particulate contamination (Beswick et al., 2008). The probe was calibrated for static and dynamic upwash (Vaughan et al., 2016, 2017). Only data collected from the Fast-AQD-NO_x, IPAS 20 and AIMMs-20 will be discussed in the study. Volatile Organic Carbon (VOC) concentration and flux data from the PTR-MS has been discussed already elsewhere (Shaw et al., 2015; Vaughan et al., 2017).

Deleted: Quantification of NO_2 mixing ratios follows an identical pathway, with an added conversion step. Ambient NO_2 is first photolytically converted to NO using a blue-light converter. The converter consists of a Teflon block containing a milled cavity (10 mL volume) down its centre, and three 395 ± 20 nm wavelength LED positioned on either side (Reed et al., 2016). Below 400 nm NO_2 photolytically degrades to NO and ground-state molecular oxygen ($O[^3P]$). The converter is cooled using a Peltier cooler to reduces thermal interference products and exhibits a conversion efficiency of >85 % and residence time of 0.11 s. After conversion, detection is achieved using the same ozone-chemiluminescence reaction as NO. Chemiluminescence detection is achieved using dry-ice cooled (-60 °C) photomultiplier tubes (PMTs) (Hamamatsu Photonics K. K.) with a red-window filter. ¶
¶ ... [1]

Deleted: ,

Deleted: i

Deleted: methodology

Deleted: ,

Deleted: g

Deleted: for NO and NO_2

Deleted: .

Deleted: Instrument precision was quantified by assessing th ... [2]

Deleted: 1

Deleted: By taking the root sum of the squares of all accuracy and precision errors

Deleted: 1

Deleted: 00

Deleted: t

Deleted: 54.5

Deleted: 88

Deleted: 3

Deleted: For 1 ppb, the total uncertainty for NO and NO_2 is 5.9% and 13.5% (at 9 Hz acquisition rate).

Deleted: a PICARRO greenhouse gas analyser,

Deleted: Aventech Research Inc.

Deleted: s

Deleted: es

Deleted: collected by

Deleted: ¶

2.3 Eddy Covariance with Environmental Response Functions

Environmental Response Function (ERF) is a physics-guided flux data fusion designed to create a bridge from EC measurements to model grid-scale flux estimates (Metzger, 2018; Metzger et al., 2013; Xu et al., 2017, 2018). In ERF, high-rate time-frequency wavelet decomposition and flux footprint modelling are used to create a time-aligned dataset between response (flux) and driver (e.g., concentration, building height etc.) observations. From this time-aligned dataset, machine learning extracts a driver-response process model – outputting a multi-dimensional surface that connects flux to process. ERF then uses this driver-response process model to project flux maps with hourly and sub-kilometre resolution, extending the areal representation of the airborne NO_x fluxes from few square kilometres around the flight tracks to the GLR. The following subsections detail the software used for ERF EC data processing and the principal processing steps.

2.3.1 Flux processing overview

NO_x fluxes were calculated using the wavelet eddy covariance (EC) approach discussed by Metzger et al. (2013), which has been described in detail elsewhere (Karl et al., 2013; Misztal et al., 2014; Thomas and Foken, 2007; Torrence and Compo, 1998; Wolfe et al., 2015; Yuan et al., 2015). Flux processing was achieved in R using eddy4R, as discussed by Metzger et al., (2017).

The eddy4R flux processing followed the workflow shown in Fig. 2. Individual transects were processed separately, with a minimum flight distance of 15 km, ensuring large atmospheric transport scales were captured. Data periods containing sharp turns or orbital loops were omitted. Meteorology, position and concentration data were merged for each transect, giving a regularised data frame at 20 Hz. Each transect was screened for data outside of defined thresholds and omitted. Overall data pass rate was set to ≥ 90 %. Successful transects underwent de-spiking using the method outlined by Brock (1986) in the form of Starkenburg et al. (2016) for wind vectors (u,v,w), temperature and NO & NO_2 mixing ratios. The technique is sensitive to up to 4 consecutive data spikes. High-pass filtered cross-covariance maximisation (Hartmann et al., 2018) was applied to correct NO/NO_2 mixing ratios and air temperature for differences in sampling time compared to the vertical wind (w). Once lag-time corrected, data was resampled from 20 Hz to 9 Hz using mean rolling averaging (Zeileis and Grothendieck, 2005).

Deleted: 2
Deleted: c
Deleted: ¶
Deleted: 2
Deleted: eddy4R eddy-covariance software
Deleted: Flux processing was achieved using the eddy4R software. The eddy4R family of R packages (Core Team, 2019) creates a modular function-based software solution for EC data processing, as described in Metzger et al., (2017). A development and systems operation approach (DevOps) was utilised to create reproducible, open-source, and extensible software that is version controlled. This DevOps schema enables a release and iteration cycle that, to date, has yielded the eddy4R.base, eddy4R.qaqc, and eddy4R.stor packages on a publicly available GitHub repository (Metzger et al., 2019; Xu et al., 2019). This modular framework facilitates scientific community-driven code development that extends the eddy4R software suite's capabilities. In the present study, we extended eddy4R to handle fluxes from a wide variety of chemical species by adding to the eddy4R.turb package that is currently in development.¶
To ensure portability and reproducibility, the eddy4R packages integrate into a Docker image, which builds upon a Linux computational environment and resolves all system and R dependencies (https://www.docker.com/why-docker). The Docker image hardens the code against operating system-induced anomalies and streamlines the code base to the essential requirements for processing. GitHub automatically triggers, and version controls Docker image builds, which are housed on Dockerhub. Continuous integration testing through Travis-CI and subsequent code reviews complete the build chain. This fosters rapid code development across teams and functionalities while mitigating unintentional errors that could corrupt the main codebase. The eddy4R-Docker DevOps framework thus provides a foundation for the distributed development of novel algorithmic solutions and their scalable execution. The described approach provides the end-user with a practical approach towards version control and result reproducibility.¶
2.2.2 Wavelet time-frequency decomposition¶
The
Deleted: ion
Deleted: was based on the
Deleted: and has been
Deleted: using
Deleted: the
Deleted: software
Deleted: , which is a family of R packages (Core Team, 2019) which create a modular function-based software solution for EC data processing, as described in
Deleted: ¶
Wavelet EC uses continuous wavelet transformation (CWT) to extract time-frequency or space-wavenumber information fro... [3]
Deleted: F
Deleted: in eddy4R f
Deleted: 3
Deleted: were

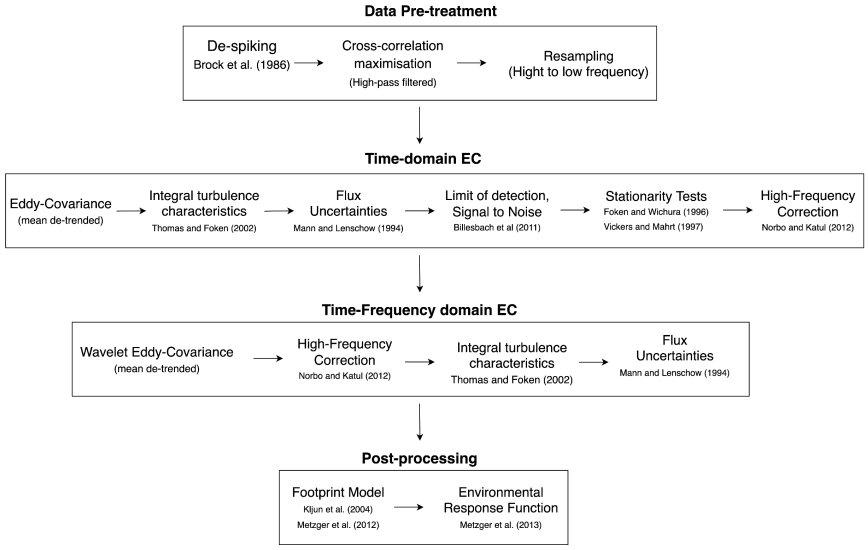

Figure 2. Modular eddy4R workflow giving four processing steps: raw data pre-treatment, time-domain EC, time-frequency-domain EC, and post-processing analysis (footprint and ERF).

After data pre-treatment, time-domain (classical) and time-frequency domain (wavelet) fluxes were calculated as outlined in Fig. 2. Time-domain EC gives a single flux estimate per transect, whereas time-frequency EC gives a flux measurement every 400 m along the transect using an overlapping 4000 m moving window. Time-frequency EC using CWT for flux analyses. A minimum wavelet scale of 4.5 Hz (Nyquist frequency) and a maximum scale of 512 s was chosen for the wavelet calculations. 512 s was chosen to ensure all long scale transport processes were accounted for, as shown in Fig. S4, whereby scales above this point don't show significant emission structure. Wavelet cone of influence was not removed in accordance with Metzger et al., (2013). Table 2 outlines eddy4R processing parameters.

Deleted: 3

Deleted: ¶

Deleted: 3

Deleted: 3

Deleted: A wavelet δj value of 1/8 and a minimum wavelet scale of 4.5 Hz (Nyquist frequency) was chosen for wavelet calculations.

eddy4R parameter	Setting
Data Frequency	9 Hz
Transect length	> 15 km
De-spiking	Median filter (Brock, 1986; Starkenburg et al., 2016)
Lag correction	High-pass filtered cross-correlation maximisation (Hartmann et al., 2018)
De-trending	mean
High-Frequency Correction	Yes (Nordbo and Katul, 2013)
Wavelet waveform	Morlet
Wavelet δj	1/8
Wavelet maximum scale	512 s
Wavelet COI inclusion	yes
Flux subinterval window	4,000 m
Flux spatial averaging	400 m

Table 2. List of eddy-covariance parameters for quantifying airborne NO_x fluxes.

Each flight leg underwent the following QA/QC steps. Each flight transect was screened for the presence of a clear cross-covariance peaks for; NO, NO_2 and temperature (Fig. S3). Limit of detection (LOD) (Billesbach, 2011) and signal to noise (S/N) statistics (Foken and Wichura, 1996; Vickers and Mahrt, 1997) were calculated and median flux LODs were found to be 0.19 mg m^{-2} h^{-1} for NO and 0.57 mg m^{-2} h^{-1} for NO_2. Fluxes below these thresholds were flagged. Median S/N statistics for NO and NO_2 fluxes were found to be 14.54 and 17.26. Stationarity tests were calculated for each flight transect, with a flag threshold of 100% used (Foken and Wichura, 1996; Vickers and Mahrt, 1997). Nine out of 42 transects failed the stationarity criteria and so were omitted. NO and NO_2 fluxes were assessed for high-frequency spectral loss using a wavelet-based correction methodology (Nordbo and Katul, 2013). Average high-frequency loss factors for NO and NO_2 were found to be 1.014 and 1.015. As these corrections increased fluxes by only 1.4 - 1.5 %, they were not applied. A detailed overview of chemical and meteorological NO_x flux losses can be found in Vaughan et al. (2016). As a final QA/QC filter, friction velocity (u*) was chosen as a metric of developed turbulence. A u* threshold of 0.15 m s^{-1} was chosen in line with other urban EC studies (Langford et al., 2010; Squires et al., 2020), with data falling below this value being filtered out.

Deleted: 1

Deleted: Presence of a

Deleted: f

Deleted:

Deleted: 4

Deleted: 15

Deleted: ¶

2.3.2 Footprint model

To assess the spatial influence of each flux, we used a footprint model. The model calculates a spatial representative weighting matrix for each measurement along the flight track. In this study, we apply a model capable of assessing influence from prevailing wind and crosswind (Metzger et al., 2012). The model uses a parameterised version of the Kljun (KL04) backwards Lagrangian model (Kljun et al., 2002, 2004), capable of calculating footprint estimates under stable and strongly convective conditions. Parameterisation was achieved using measurement height (Z_m), u*, standard deviations of vertical and horizontal wind speeds, the planetary boundary layer height (Z_i) and aerodynamic roughness length (Z_0). We used previously published Z_0 values for the GLR, accounting for westerly and easterly wind influences, at 1 km^2 resolution (Drew et al., 2013). The model generates a weighting matrix across the same domain as the spatial dataset of interest, summing up to one and is centred on the aircraft's location. The footprint matrix can then be used to weight and cumulative sum the spatial dataset, giving a representative value along the flight leg. Fig. 3 shows the average calculated footprint across the campaign at 30, 60, and 90% influence contours. On average, the 90% influence distance ranged from 3 - 12 km.

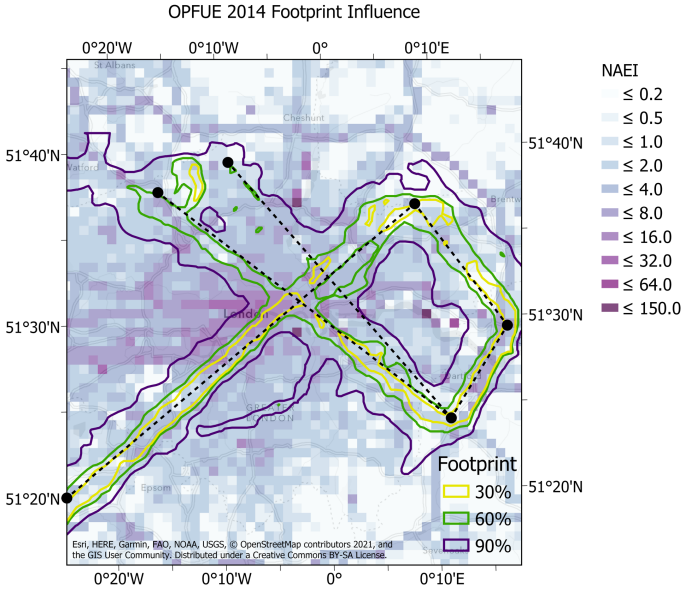

Figure 3. Footprint climatology of all aircraft transects, indicated by the 30, 60, 90% contour lines of the cumulative surface influence superimposed over the 2014 NAEI for NO_x emissions in Tons km^{-2} yr^{-1}. Plotted in ArcGIS® (Esri, 2021b).

2.3.3 Boosted regression tree machine learning

Linking time-of-day measured fluxes at the aircraft transect height to the surface can be challenging and is driven mainly by their spatio-temporal variability. The application of an ERF, in contrast, can bridge this gap by building relationships between measured flux (spatial and temporal) and environmental drivers. We used boosted regression trees (BRT) (Elith et al., 2008; Metzger et al., 2013; Serafimovich et al., 2018) to calculate ERF relationships between measured airborne fluxes (spatial and temporal) and multiple environmental drivers. BRT is a non-parametric machine learning technique that combines regression trees and boosting to formulate ERF relationships (Serafimovich et al., 2018). BRT parameters were determined using the same strategy as Metzger et al., (2013), through the cross-validation procedure described in Elith et al., (2008). We found by using a learning rate of 0.1, tree complexity of 6, bag fraction of 0.75, absolute (Laplace) error structure and $3.7e^4$ trees overall, we were able to minimise the predicted deviance whilst achieving the optimum model fit. The BRT approach used an initial 500 trees, with 500 trees added at each step. The training dataset consisted of 1,751 airborne flux observations after QA/QC filtering.

3 Results and discussion

3.1 Airborne NO_x fluxes

NO_x fluxes were calculated during four flights, giving 11 complete transects across the GLR and 2884 individual 400 m flux averages. Measurements were made at a relatively constant altitude above the surface (340 ± 40 m), corrected for both terrain elevation and building height. Building height data for the entire Greater London region was obtained from Digimap Ordnance Survey Web Map Service (Digimap) (Ordnance Survey, 2020). To account for changing boundary layer heights, we used hourly 0.25-degree estimates from the ERA5 fifth-generation ECMWF reanalysis for global climate data (Hersbach et al., 2018). The calculated depth of the boundary layer (Z_m/Z_i) ranged from 0.150 to 0.770, with a median Z_m/Z_i of 0.255. Atmospheric stratification was found to be mostly unstable throughout the campaign, with a median Obukhov length (L) of -182 m and dimensionless Monin-Obukhov stability parameter (Z_m/L) of -1.98. Friction velocities ranged from 0.06 to 1.09 m s^{-1}, with an average of 0.56 m s^{-1}.

EC measurements are affected by random and systematic uncertainties. Random error accounts for uncertainty due to insufficient averaging period, resulting in the inadequate sampling of primary contributing eddies (Lenschow et al., 1994; Mann and Lenschow, 1994). A detailed review of random error estimation approaches for EC can be found in Salesky et al. (2012). Systematic error accounts for under-sampling of the largest atmospheric scales responsible for turbulent flux (Lenschow et al., 1994; Mann and Lenschow, 1994). At a 400 m averaging interval, the median random error (± median absolute deviation) for the NO flux was 126.6 ± 80.6 % and 108.3 ± 58.5 % for NO_2. The median systematic error for NO and NO_2 flux were 14.7 ± 4.7 % and 14.3 ± 4.5 %. Chemical loss of NO_x to OH was not corrected for in this study, which is in line with the discussion in Vaughan et al. (2016), with such losses being small (1 – 2%).

Deleted: ¶
¶
Deleted: 2
Deleted: 5
Deleted: which
Deleted: (
Deleted:
Deleted: Metzger et al., (2013),
Deleted:
Deleted: Calculated
Deleted: errors
Deleted: ,
Deleted: in the range of
Deleted: median random error for the NO flux was 126.6 % and 108.3 % for NO_2. The median systematic error for NO and NO_2 flux were 14.7 % and 14.3 %.

As the Fast-AQD-NO_x quantifies mixing ratios of NO_x in wet air, the effect of density fluctuations (WPL) on calculated NO_x flux was assessed using the method described by Hartmann et al., (2018), Eq.21. Fast (20 Hz) mixing ratios of water vapour were calculated from; relative humidity, pressure, and temperature data, and corrected for lag-time differences to the vertical wind. The water vapour mixing ratio was used to convert NO/NO_2 mixing ratios to dry mole before performing EC calculations. Fig. S6a shows the linear regression between uncorrected and corrected NO_x flux for the influence of WPL. Correcting for WPL increased measured NO_x flux on average by 1.35%. In addition to WPL corrections, the effect of vertical flux divergence was also investigated. Vertical divergence can account for significant flux losses due to weakening vertical momentum at increased altitudes below the planetary boundary layer (Deardorff, 1974; Sorbjan, 2006). Fig. S6b shows corrected vs uncorrected NO_x flux using the method outlined by Sorbjan (2006), showing a potential 50% flux increase. Due to the coarseness of the ERA5 PLB data at 0.25-degree resolution and the complexity of London's surface structure, a more detailed assessment is needed to understand what potential effects vertical flux divergence may have on urban emission estimates. Due to strict air traffic control restrictions, vertical profiles were not possible during the campaign, which would have allowed for a more detailed assessment of divergence influences. The NO_x fluxes reported in this study are not corrected for vertical flux divergence, and so will be considered as conservative due to the listed processes having the potential to further increase measured rates.

Flux measurements were made across a 5 day period, giving 3 weekdays (Mon-Wed) and 1 weekend day (Saturday). The temporal distribution of measurements is well distributed, ranging from 08:00 to 16:00 UTC. Hourly averaging across the entire dataset shows a partial diurnal profile, with the maximum hourly mean NO_x flux for the GLR occurring at 10:00 (8.95 mg m^{-2} hr^{-1}). The diurnal profile does not extend past 16:00, due to encountered air traffic control time restrictions. The present diurnal is complex due to limited flight hours and the spatial variation of measured fluxes. Focus on the temporal component, fluxes were hourly bin averaged and grouping according to the flight leg type (Fig. 1) and measurement location with 3 defined areas: central London, North/South Circular area and outer London. Fig. 4 shows hourly boxplot flux averages for each flight leg type vs location in London. Leg 1 showed a strong morning diurnal for Central and North/South Circular areas of London, compared to legs 2 & 3, which typically showed consistent NO_x emission rates across the different hours sampled. Emissions measured during the hours of 08:00-10:00 UTC in central London are above 20 mg m^{-2} h^{-1}, which is consistent with other London studies assessing London emissions (Lee et al., 2015). The temporal variability of leg 5 was contrastingly different to the other 4 legs and is heavily influenced by road transport emissions (M25 orbital motorway).

Deleted: ,…and corrected for lag-time differences to the vertical wind.,.…The and…ater vapour mixing ratio then…as used to correc…vert NO/NO_2 mixing ratios to dry mole before performing EC calculations. Fig. S6a shows the linear regression between uncorrected and corrected NO_x flux for the influence of WPL. Correcting for WPL increased measured NO_x flux on average by 1.35%, on average… In addition to WPL corrections,.,…the effect of vertical flux divergence was also investigated. In addition to density and chemical loss processed,… v…rtical divergence can also account for significant flux losses,…due to weakening vertical momentum at increased altitudes below ... [4]

Deleted: estimated ERA5 fifth-generation ECMWF reanalysis boundary layer height… showing a potential 50% flux increase. Due to the coarseness of the ERA5 PLB data at 0.25-degree resolution and the overall …omplexity of London's surface structure, a more future …ssessment is needed to understand what the …otential effectss…vertical flux divergence may have on urban emission estimates. Due to strict air traffic control restrictions, , as detailed vertical profiles were not possible during the campaign, which would would have allowed for a more detailed assessment of divergence influences due to air traffic control restrictions… The NO_x fluxes reported in this study are not corrected for vertical flux divergence, and so will be considered as conservative due to the listed processes having the potential to further increase measured rates.e. ... [5]

Moved (insertion) [1]

Deleted: over…cross a 54…day periods… giving 3 weekdays (Mon-Wed) and 1 weekend day (Saturday). The temporal distribution of measurements is well distributed, ranging from 08:00 to 16:00 UTC. Hourly averaging across the entire dataset shows a partial diurnal profile, with the maximum hourly mean NO_x emission…lux for the GLR occurring at 10:00 (8.95 mg m^{-2} hr^{-1}). The diurnal profile does not extend past 16:00, due to encountered air traffic control time restrictions across the GLR… The present diurnal is complex due to limited flight hours and the spatial distribution…ariation of measured fluxes in highlight heterogeneous terrain… To reduce the spatial variability between measurements and …f…cus on the temporal component,… fluxes were hourly bin averaged and by…grouping according to the flight leg types…(Fig. 1) and data…easurement location with within ... [6]

Deleted: NO_x …verages for each flight leg …type vs location in Londonagain three areas of London… Leg 1 showed as a…strong morning diurnal structure …or Central and North/South Circular areas of London, compared to legs 2 & 3, which typically showed consistent NO_x emission rates across the different hours sampled. Emissions measured during the hours of 08:00-10:00 UTC in central London are above 20 mg m^{-2} h^{-1}, which is consistent with other London studies assessing London emissions (Lee et al., 2015). The temporal variability of leg 5 was contrastingly different to the other 4 legs types …nd is heavily dependent…nfluenced by on measured emissions in a …oad transport dominated domain ... [7]

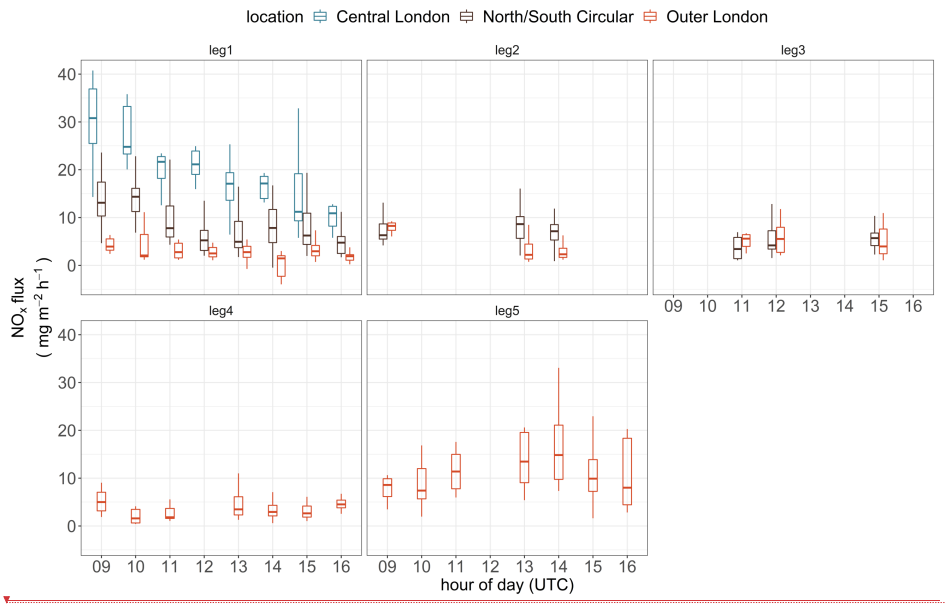

Figure 4. Hourly boxplots analysis of measured NO_x fluxes, grouped by flight leg type and location within London. Grouping have been defined as the following. Central London (51.48º N - 51.52º N, 0.17º W - 0.07º W). North/South Circular (51.44º N – 51.6º N, 0.29º W – 0.07º E), excluding the Central London area within. Outer London (51.25º N – 51.7º N, 0.54º W – 0.29º E) excluding both Central London and North/South Circular areas within.

By aggregating and averaging across multiple transects, the temporal variability can be better accounted for, giving a clearer picture of the spatial component. Fig. 5 shows mean 400 m latitude flux averages for each of the five transect types. The shaded area shows the average flux random error divided by the square root of the number of sample points which went into each mean. Averaging reduces the individual flux uncertainty (>100%), with the average flux uncertainty (average error/sqrt(n)) being 48.7 ± 20.7 %. Transect 1 follows an identical path to that of similar measurements made previously in 2013 and shows comparable NO_x fluxes (Vaughan et al., 2016). The highest observed fluxes (>20 mg m^{-2} hr^{-1}) were measured over the London Borough of Southwark and the City of London. Both areas include major roads, national rail stations and densely packed high-rise buildings, giving profoundly heterogeneous emission sources of NO_x. Transects 2 & 3 (Fig. 5) ran perpendicular to transect 1, giving emission information over the Southeast and Northwest areas of Greater London. The emission structure of transect 2 shows similarities to that of transect 1, with fluxes in the central area above 10 mg m^{-2} h^{-1}. Transect 3, in comparison, showed 50% lower emissions (5 mg m^{-2} h^{-1}). This transect was over more suburban areas compared to transects 1 and 2. The final

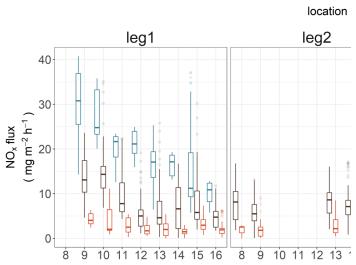

Deleted:

Deleted: emissions

Deleted: The location g

Moved up [1]: Flux measurements were made over 4 days, giving 3 weekdays (Mon-Wed) and 1 weekend day (Saturday). The temporal distribution of measurements is well distributed, ranging from 08:00 to 16:00 UTC. Hourly averaging across the entire dataset shows a partial diurnal profile, with the maximum hourly mean NO_x emission for the GLR occurring at 10:00 (8.95 mg m^{-2} hr^{-1}). The diurnal profile does not extend past 16:00 due to air traffic control time restrictions across the GLR. The present diurnal is complex due to limited flight hours and the spatial distribution of measured fluxes in highlight heterogeneous terrain. To reduce the spatial variability between measurements and focus on the temporal component, fluxes were hourly bin averaged by grouping according to the flight leg types (Fig. 1) and data within: central London, North/South Circular area and outer London. Fig. 4 shows hourly boxplot NO_x averages for each flight leg again three areas of London. Leg 1 shows a strong morning diurnal structure for Central and North/South Circular areas of London, compared to legs 2 & 3, which typically showed consistent NO_x emission rates across the different hours sampled. Emissions measured during the hours of 08:00-10:00 UTC in central London are above 20 mg m^{-2} h^{-1}, which is consistent with other London studies assessing London emissions. The temporal variability of leg 5 was contrastingly different to the other 4 leg types and is heavily dependent on measured emissions in a road transport dominated domain (M25 orbital motorway).¶

Deleted: ¶
¶
¶
... [8]

Deleted: e

Deleted: of the measured fluxes

Deleted:

Deleted: 5

Deleted: , with the shaded area the standard deviation of the calculated mean

Deleted:

Deleted: 5

Deleted: E

Deleted: W

transcripts (4 and 5) ran over eastern parts of the GLR, extending out to the M25 Orbital Motorway and industrial infrastructure. The Dartford Crossing (A282) area showed elevated NO_x emissions (>10 mg m^{-2} h^{-1}). It was evident during most flights that this area was prone to congestion, suggesting vehicles as the primary source. The design capacity of the bridge is 135,000 vehicles per day, but vehicle flows now routinely exceed 160,000 per day.

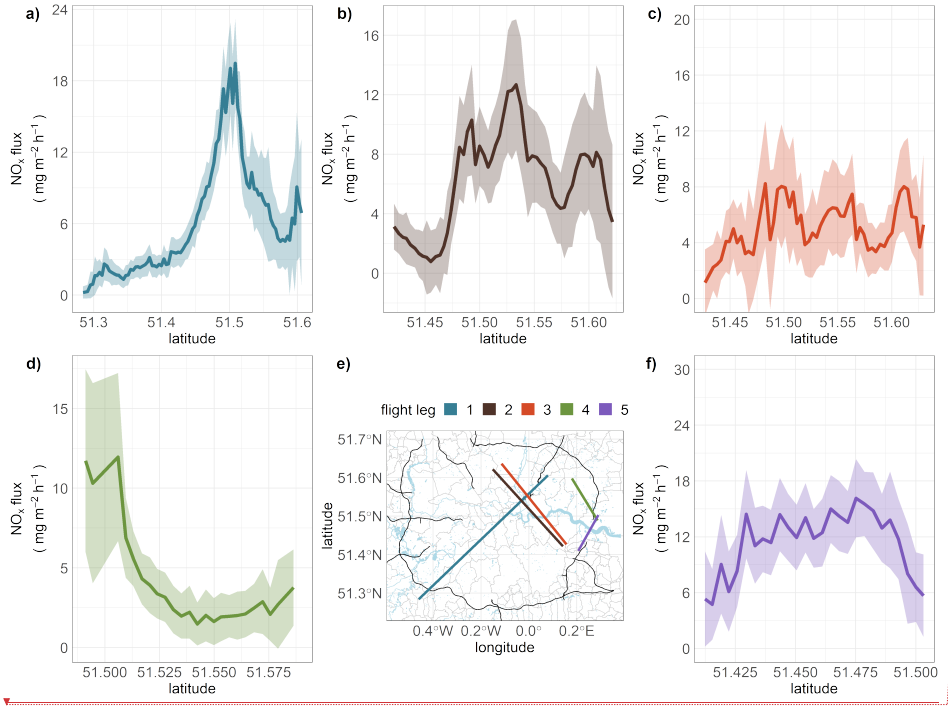

Figure 5. Ensemble NO_x flux flight track averages (400 m) across the campaign, with the shaded area representing the average random error divided by the square root of the number of sample points which went into each mean (error/sqrt(n)). The top row (a, b & c) shows flight transects 1, 2 and 3 which ran over central areas of London such as City of London Borough. The bottom row (d & f) transects 4 and 5, ran over eastern regions of Greater London, home to industry and major road network. e) shows each individual track transect overlaid onto the OpenStreetMap's; major road infrastructure, local boundaries, and rivers around the GLR (OpenStreetMap contributors, 2021; Padgham et al., 2020).

Deleted:

Deleted: 5

Deleted: 400 m

Deleted: Ensemble 400 m NO_x flux flight track averages across the OPFUE 2014 campaign.

Deleted: .

Deleted: The shaded area represents the standard deviation of the ensemble mean.

Deleted: .

Deleted: e) shows each individual track transect overlaid onto major road infrastructure, local boundaries, and rivers around the Greater London Region. Map was built using data from © OpenStreetMap contributors 2021. Distributed under a Creative Commons BY-SA License.

Deleted: ¶

3.2 Comparison to Emission Inventory

Measured fluxes are a powerful tool for evaluating bottom-up emission estimates, such as the NAEI. The NAEI is vital for assessing UK air quality, providing annual emissions estimates for a range of pollutants at 1 km^2 resolution for the UK region. Each pollutant has an individual bottom-up inventory, covering hundreds of different emissions categories, which, when summed together, give an annual national estimate. These sources include; road transport, domestic and industrial combustion, rail, aviation, energy generation, waste, fossil fuel extraction and agricultural production. The NAEI's road transport sector is based on emissions UK road traffic statistics and the COPERT (Calculation of Emissions from Road Transport) 4 emission factor model, which is part of the European Monitoring and Evaluation Programme/European Economic Area (EMEP/EEA) air pollutant emission inventory guidebook (Bush et al., 2008; EEA, 2013). For each airborne flux, a footprint matrix was generated at the same spatial extent and resolution (1 km^2) as the NAEI, using the described footprint model. Each footprint equates to a value of one and weights each grid cell of the NAEI individually. Once weighted, all cells are summarised, giving a spatially representative emission estimate. We corrected for time-of-day emission variations by scaling each source sector individually for monthly, daily and hourly influences using factors unique to each sector. Once scaled, all sources are summed to produce a time-of-day estimate, comparable to the location and time-of-day each flux measurement was made.

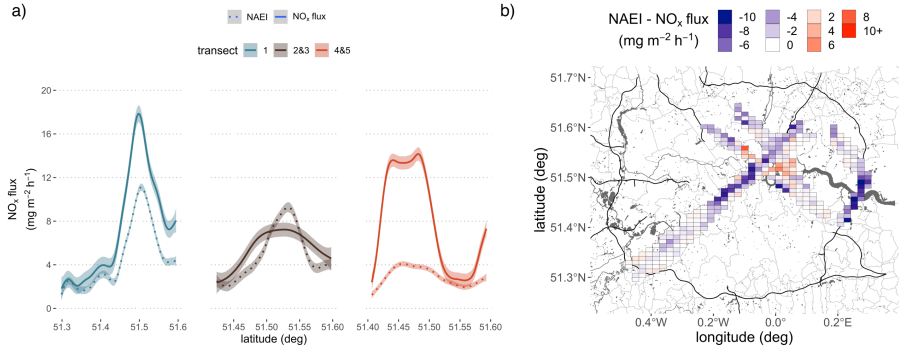

Figure 6. a) Transect grouped NO_x flux and NAEI emission estimates as a function of latitude. A generalised additive model (GAM) has been fitted to each transect grouping, using a k value of 10. The 95% confidence interval of the GAM is shown as the light shaded area. b) Spatially median binned 1 km^2 difference between predicted NO_x emissions (NAEI) and measured NO_x fluxes, mapped onto the OpenStreetMap's; major road infrastructure, local boundaries, and rivers around the GLR (OpenStreetMap contributors, 2021; Padgham et al., 2020).

Deleted: For each airborne flux, a footprint matrix was generated at the same spatial extent and resolution (1 km^2) as the NAEI. Each footprint equates to a value of one and weights each grid cell of the NAEI individually. Once weighted, all cells are summarised, giving a spatially representative emission estimate. We corrected for time-of-day emission variations by scaling each source sector for monthly, daily and hourly influences. Once scaled, all sources are summed to produce a time-of-day estimate.

Deleted: ¶

Deleted: measured

Deleted: es

Deleted: , and the

Deleted: Transect grouped measured NOx fluxes and NAEI emission estimates as a function of latitude. A generalised additive model (GAM) has been fitted to each transect grouping, using a k value of 10. b) Spatially median binned 1 km2 difference between predicted NOx emissions (NAEI) and measured NOx fluxes, mapped onto major road infrastructure, local boundaries, and rivers around the Greater London Region. Map was built using data from © OpenStreetMap contributors 2021. Distributed under a Creative Commons BY-SA License.¶

To compare measured fluxes against footprint calculated time-of-day NAEI estimates, each transects type was 1 km mean binned as a function of latitude. Transects 2 and 3 were grouped to produce a perpendicular comparison to transect 1. Transects 4 and 5 were grouped to give a comparison in an area more representative of industrial/road transport-dominated emission sources. Fig. 6a shows the measured flux (solid) and time-of-day scales NAEI estimates (dotted) as a function of latitude for each of the three groupings using a generalised additive model (GAM) fit (Hastie and Tibshirani, 1990). The GAM fits a non-linear distribution to the data, being either the measured flux or time-of-day inventory estimate as a function of latitude. The shaded area shows the 95% confidence interval of the GAM fit. Measured fluxes along transect 1 consistently showed higher NO_x emissions than estimated by the NAEI (mean of 1.5 times higher). The greatest divergence ratio between the measured and inventory-estimate fluxes was 1.98, which is broadly consistent with previous studies (Lee et al., 2015). The divergence for transect 1 was most substantial when a mix of different emission sources were encountered, such as other transport mediums (rail and shipping) and, domestic and industrial combustion settings (see Table 3). Comparison for grouped transects 2 and 3 showed improved agreement to the inventory, with measured fluxes on average 1.21 times higher. The percentage contribution of emissions sources was similar to transect 1, with only a slightly lower average road transport contribution (63%). The stronger agreement between transects 2 and 3 suggests the high emissions observed during transect 1 are dependent on either a missing or under-represented source in the inventory. Grouped transects 4 and 5 also displayed a high degree of divergence from the inventory. On average, the ratio between measurement and inventory was 2.57, with a peak value of 4.45. The primary sources for this area include a greater contribution from energy production and industrial combustion. Table 3 summarises the three different groups, with average NAEI sector contributions and the ratio between flux measurement and inventory.

Transect	Road Transport	Other Transport	Domestic Combustion	Industrial Combustion	Energy Production	Ratio (Flux/NAEI)
1	63.89 %	9.24 %	21.71 %	4.27 %	0.82 %	1.51 ± 0.31
2 & 3	62.75 %	8.44 %	22.2 %	6.06 %	0.42 %	1.20 ± 0.27
4 & 5	70.09 %	8.47 %	11.1 %	8.40 %	1.90 %	2.58 ± 1.39

Table 3. predicted NAEI emission sources group by transect time and the median ratio of measurement to NAEI estimate (± median absolute deviation). These sources are; road transport, other transport such as rail and shipping, domestic combustion (combustion in commercial, institutional, residential and agriculture), industrial combustion (combustion in industry) and energy production (combustion in energy production and transformation).

Spatially, the disagreement between measurement and inventory is uneven, as shown by Fig. 6b, whether, for each 1 km along the flight track, the median inventory minus measurement value has been calculated. South-western areas of the GLR agree better than the central and north-eastern areas. Greater under-estimation by the inventory compared with measurements was predominantly observed in regions of complex source distribution and where no single primary source dominated. The extent

Deleted: spatially representative NAEI estimates,
Deleted: ,
Deleted: ted
Deleted: Fig. 6a shows measured, and NAEI estimates as a function of latitude for each of the three groupings, with a generalised additive model (GAM) fitted
Deleted: of choice
Deleted: in this case
Deleted: to the data
Deleted: one
Deleted: that of
Deleted: dependant
Deleted: for
Deleted: r
Deleted: 4
Deleted: 23
Deleted: 31
Deleted: 04
Deleted: Transect grouping of NAEI
Deleted: percentage
Deleted: contribution by five key sources
Deleted: mean

of disagreement highlights the challenges and consequent drawbacks of using the NAEI as a predictive tool for estimating NO_x emissions or as a time-of-day diagnostic for measured NO_x fluxes. Several vital processes may likely contribute to the observed differences, in addition to NO_x emissions being higher than in the NAEI. The first is inventory scaling from annual to time-of-day. As each source sector undergoes individual scaling, these factors play a significant role in predicting time-of-day influences. Currently, these factors lack spatial disaggregation and do not account for the unique temporal profiles present per area. In contrast to the NAEI, the London Atmospheric Emissions Inventory (LAEI) uses emissions data from individual vehicle classes, obtained by on-the-road 'remote-sensing', to constrain its predicted emissions from the road transport sector, giving a more realistic comparison to "real life" emissions and hence to eddy-covariance measurements (Lee et al., 2015; Vaughan et al., 2016).

3.2 Spatio-temporal emissions

To overcome the limitation of using time-of-day representative NAEI estimates to explain measured fluxes, a more pragmatic approach was chosen. Using the outlined ERF methodology, we attempted to generate representative emission grids for each flight transect. To train the BRT technique, NO_x flux data was filtered to include 0.5 to 99.5% quantile values and positive fluxes only. We found excellent agreement between measured and ERF reproduced NO_x fluxes in the range of 0 - 37 mg m^{-2} h^{-1}. The two datasets agreed close to a 1:1 trend (0.96), with an R^2 coefficient of correlation of > 0.99 and a residual standard deviation of 0.01. Fig. S7a shows the linear regression between median averaged measured flux vs BRT model prediction for each flight transect.

Six environmental drivers were used in the ERF process to describe the spatio-temporal nature of the measured NO_x fluxes. Fig. 7 shows the partial response functions calculated for each driver against difference from the mean flux and ranked in terms of percentage contribution to the flux distribution. Two different spatial datasets were used to account for the complex heterogeneity of the Greater London Region (Fig. 7a & c). Using the described footprint methodology, spatially representative surface NO_x concentrations and building heights were calculated for each flux from the LAEI and Ordnance Survey datasets (Greater London Authority, 2013; Ordnance Survey, 2020). Preliminary analyse using surface NO_x concentration as the only spatial driver appeared to overweight suburban areas and underweight central areas of the GLR. The combination of the two datasets helps to reinforce the significant spatial differences between outer and inner London. To account for meteorological differences, NO_x concentration at altitude (Fig. 7b), relative measurement height in the boundary layer (Z_m/Z_i) and potential temperature were chosen as ERF drivers (Fig. 7e & f). As shown in Fig. 7e, 90% of flight data occurs below a Z_m/Z_i value of 0.4, with the function above 0.4 being mainly linear. Solar azimuth angle (Fig. 7d) was chosen to account for temporal variations in the measured flux. Flight data is well distributed across the solar azimuth angle domain from 100 to 260°, corresponding to 08:00-16:00 UTC.

Deleted: ,
Deleted: on
Deleted: 9
Deleted: the
Deleted: NO_x flux
Deleted: Greenwich Mean Time (GMT).

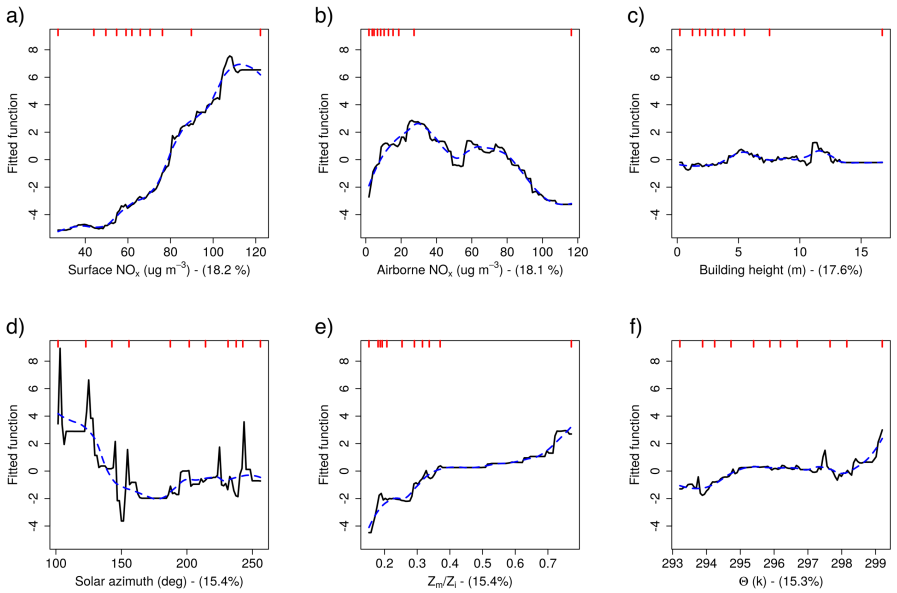

925

Figure 7. Partial dependency plots for six environmental drivers, showing BRT-fitted ERFs (black line) for each driver as a function of flux dependency from the mean, and are ranked in terms of percentage contribution (%) towards accounting for NO_x flux distribution. The red degree marks on the top x-axis show the data distribution from 0-100% in 10% bins. The Blue line shows the smoothed trend for each dependency plot.

930

For each flight leg, surface-layer NO_x fluxes were projected using median calculated statistics. Median values were chosen to account for the high heterogeneity across the length of a flight leg. Z_m/Z_i values for each ERF flux projection were kept constant, to enable comparison between legs. Overall, 20 unique transects were projected onto an aggregated 400 m^2 LAEI grid, marrying to the spatial resolution of measured flux. Fig. 8 shows the median average of all ERF flux projections across

935 the field campaign. Overall, ERF flux projection was possible across 98% of the GLR domain. Strong NO_x emission rates are exhibited in central London with lower emissions in outer London. The standard deviation between individual flight transects is low, showing an of ± 2.45 mg m^{-2} h^{-1}. The calculated relative standard deviation (RSD) shows a more complex picture, with predicted emissions in outer regions of London having a high RSD (>40 %) compared to central London (>35 %). Fig. 8C shows the calculated RSD across the GLR domain, suggesting central areas showed a more consistent emission profile during

940 the campaign, highlighting the need for further refinement of how the ERF predicted emissions in outer areas of London. ERF did not extrapolate onto areas of much higher or lower surface NO_x concentrations (shown as grey), which exceeded the ranges

Deleted:

Deleted: s

Deleted: Partial dependency plots for six environmental drivers, showing BRT-fitted ERFs for each driver as a function of flux dependency from the mean, and are ranked in terms of percentage contribution (%) towards accounting for NO_x flux distribution. The red degree marks on the top x-axis show the data distribution from 0 to 100% in 10% bins.

observed in the training dataset. These areas included parts of the M25 orbital motorway, due to limited data airborne over the region and where footprints extended beyond the confines of the LAEI grid. Areas of central London are also left blank due to footprints not encountering surface concentrations above 122 ug/m^3.

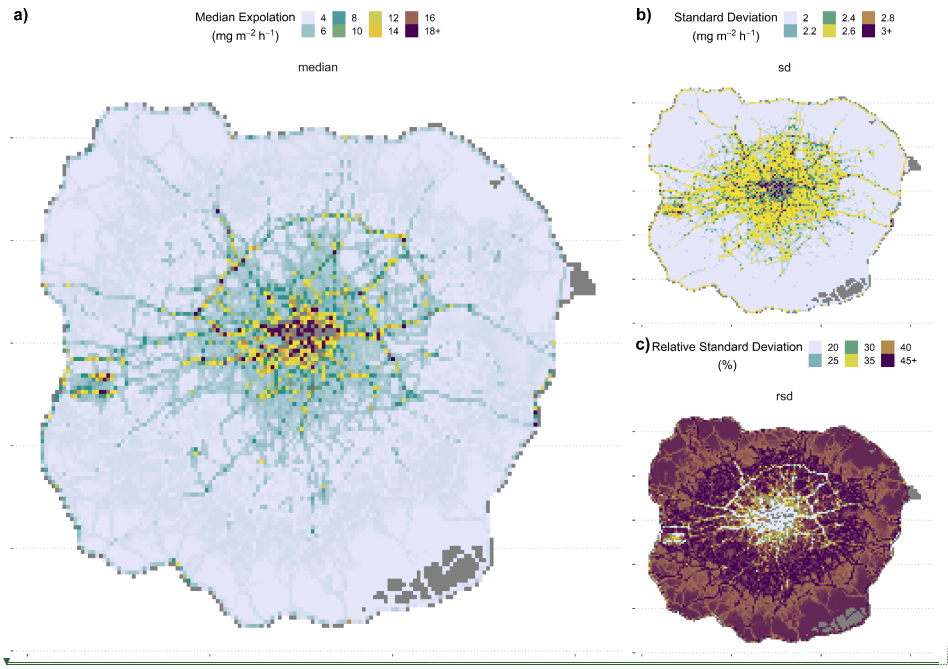

Figure 8. The median average projection of NO_x emissions (mg m^{-2} h^{-1}) at 400 m^2 resolution from all flight transect data. The standard deviation (b) and relative standard deviation (c) show the variability between individual flight transect projects. Missing areas outside of the ERF training dataset are shown in grey.

To assess the performance of the BRT model, one flight transect was omitted at a time, and the incomplete model was then used to predict the omitted dataset. Fig. S7b shows the comparison between the predicted median flight emission average using the incomplete model vs the complete. Linear regression gives a slope of 0.867, with the incomplete model, on average, overpredicted fluxes by 13.8% (0.74 mg m-2 h-1), which is taken as the prediction uncertainty of the complete BRT model. The difference between the two models is comparable to the finding of Metzger et al., (2013), which found model differences for sensible and latent heat flux to be between 11-18%, using the same technique. The spatial uncertainty distribution across

Moved (insertion) [2]

Deleted: To assess the performance of the BRT model, one flight transect was omitted at a time, and the incomplete model was then used to predict the omitted dataset. Fig. S6b shows the comparison between the predicted median flight emission average using the incomplete model vs the complete. , using the same techniquecomplex,ST generally overestimates NO_x emissions in Outer London more significantly than in ,salign more strongly. The prediction performance of the BRT model varied from flight transect to transect, as shown in Fig. S7. The majority of flight leg projects successfully scaled Central London emissions comparably to that of measured fluxes. The projects also successfully captured key features in the flux observation, such as major road networks and densely populated areas.¶

¶

¶

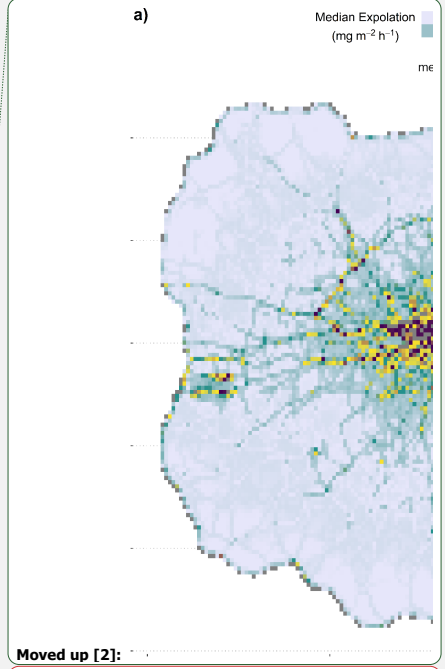

Moved up [2]:

Deleted: ¶

Figure 8. The median average projection of NO_x emissions (mg m^{-2} h^{-1}) at 400 m^2 resolution from all flight transect data. The standard deviation (b) and relative standard deviation (c) show the variability between individual flight transect projects. Missing areas outside of the ERF training dataset are shown in grey.Median (a), Standard Deviation (b) and Relative Standard Deviation (c) ERF flux projection from all individual flight legs at 400 m^2 resolution. Missing areas outside of the ERF training dataset are shown in grey.¶

the GLR is complex, as showing Fig. S7c. The incomplete model generally overestimates NO_x emissions in Outer London more significantly than in Central London, where the models align more strongly. The prediction performance of the BRT model varied from flight transect to transect, as shown in Fig. S8. The majority of flight leg projects successfully scaled Central London emissions comparably to that of measured fluxes. The projects also successfully captured key features in the flux observation, such as major road networks and densely populated areas.

The diurnal variability was also investigated during the campaign by grouping flight data into hourly bins and using the median hourly statistics to drive each ERF flux projection. Again, Z_m/Z_i was kept constant for all projections. Fig. 9 shows the average hourly ERF projections, spanning an eight-hour period from 09:00 -16:00. All projections retain a strong heterogeneous profile. The most substantial emission rates were observed during 09:00 - 10:00 (Fig. 9a-b), aligning with the morning rush-hour. The emission rates rise across the GLR, in unison, until 10:00, when emissions stabilise into the afternoon period. Projected central London emissions during this period agree well with measured fluxes, whilst more suburban areas are potentially scaled too high, suggesting further temporal refinement across the domain is required. The evening rush-hour, previously observed in NO_x emissions in London after 16:00 (Lee et al., 2015) is not captured in these predictions.

Deleted: D

Deleted: ,

Deleted: flux

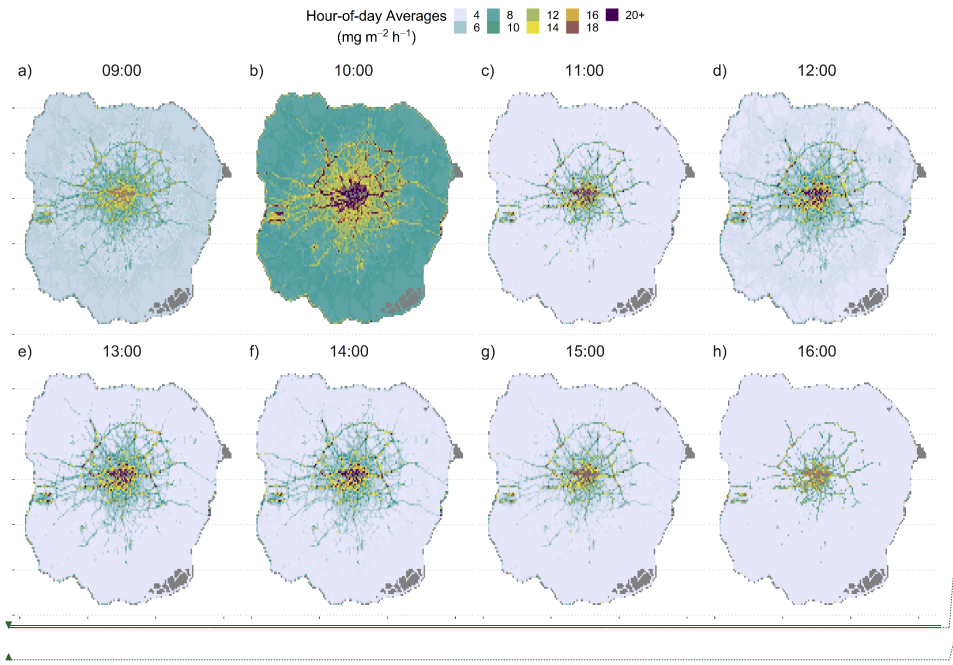

Figure 9. Hour-of-day ERF flux projections from 09:00 to 16:00. Grey colour highlight areas outside of the ERF training dataset. The strong presence of the morning rush-hour period is observed from 09:00 to 10:00 (a-b).

4 Conclusions

The assessment of NO_x emissions in urban areas remains an important area for research, due to the critical impacts that high NO_x concentrations have on local public health and the attainment of national trans-boundary emissions commitments. In this study, we used airborne measurements over the Greater London area to upscale airborne NO_x flux observations to high-resolution emission projections across the region, via Environmental Response Function (ERF) physics-guided flux data fusion. The work presented here presents a method which can quantify and spatially disaggregate NO_x fluxes over challenging urban terrain and has the potential to be applied to other metropolitan areas worldwide.

Seven low altitude research flights were made over the Greater London region (GLR) in July 2014, performing multiple over-passes across the city. From these flights, 2715 individual NO_x fluxes at 400 m spatial resolution were measured and processed

Moved (insertion) [3]

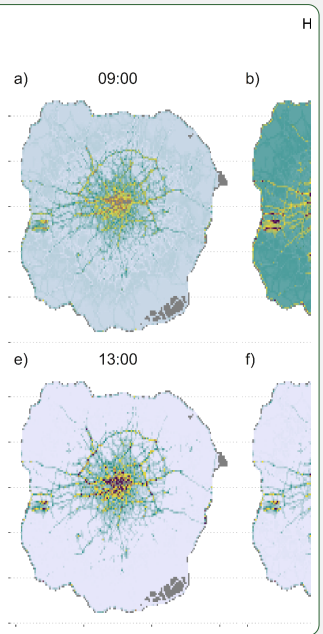

Moved up [3]:

in R using the eddy4R software. Measured NO_x fluxes across the Greater London region exhibited high heterogeneity and substantial diurnal variability. Central areas of London showed the highest emission rates quantified during the campaign. Other high emission source areas included the M25 orbital motorway. The complexity of London's emission characteristics makes it challenging to pinpoint single emission sources definitively. In practice, multiple sources are likely to contribute to measured fluxes at the spatial scale used here, including road transport and residential, commercial and industrial combustion (mainly for space heating). To give a time-of-day reference, we compared measured fluxes to the UK's National Atmospheric Emissions Inventory, scaled to account for monthly, daily and hourly differences from the annual values. We found that for central areas of London, the inventory underestimated emissions by up to a factor of two, which is consistent with other published studies. Measured fluxes were consistently higher than inventory estimates across most of Greater London.

To overcome the limitations of comparing to the national inventory, we trained ERFs between measured spatial-temporal NO_x fluxes and environmental drivers (meteorological and surface) to generate time-of-day emission surfaces. ERF successfully reproduced aircraft measured NO_x fluxes, with a coefficient of determination (R^2) of 0.99. We used the calculated ERF relationships to project the NO_x flux for the time of each flight transect across the GLR domain at 400 m^2 resolution. We were able to achieve a 98% spatial coverage and a highly heterogeneous emission surface. The overall variability between ERF flux projections was low, with an average relative standard deviation of 40%. All ERF flux projections showed high emissions emanating from central areas of London and the major road network. Hour of day projections highlighted a strong morning rush-hour, peaking at 10:00, and remaining elevated into the afternoon. Overall, the integration of high-resolution spatio-temporal fluxes with an ERF driven strategy has enabled the generation of spatial NO_x emissions at high-resolution over Greater London.

This work demonstrates the power of airborne eddy-covariance based measurements of air pollutant fluxes as a tool for evaluating emission inventories or as a method of independently obtaining spatially disaggregated city-wide emission rates of pollutants. The method is applicable to other metropolitan areas or any other heterogeneous landscape. It should also help legislating authorities better understand air pollution sources and the effectiveness of control measures.

Code availability

The eddy4R v0.2.0 software framework used to generate eddy-covariance flux estimates is described in Metzger et al. (2017) and can be freely accessed at https://github.com/NEONScience/eddy4R. The eddy4R turbulence v0.0.16 software module for advanced airborne data processing described in Metzger et al. (2013) was accessed under Terms of Use for this study (https://www.eol.ucar.edu/content/cheesehead-code-policy-appendix) and is available upon request.

Data availability

Any flux data presented here may be accessed by contacting the authors.

Author contribution

JDL, ACL, RMP, BD and CNH conceptualized the study and obtained funding. ARV, JDL, MDS, BD and CNH conducted the airborne field measurements. ARV, SM and DD analysed the eddy-covariance data and conducted the machine learning analysis. All authors reviewed and edited the paper.

Competing interests

The authors declare that they have no conflict of interest.

Acknowledgements

We thank the UK Natural Environment Research Council for financial support and the staff of the NERC's Airborne Research and Survey Facility for their enthusiasm and skill in performing our multiple low-level flights across London. The National Ecological Observatory Network is a project sponsored by the National Science Foundation and managed under cooperative agreement by Battelle. This material is based upon work supported by the National Science Foundation (grant no. DBI-0752017). Any opinions, findings and conclusions or recommendations expressed in this material are those of the author and do not necessarily reflect the views of the National Science Foundation.

Deleted: ¶

References

Aubinet, M., Vesala, T. and Papale, D.: Eddy covariance: a practical guide to measurement and data analysis, Springer Science & Business Media., 2012.

Baldocchi, D. D.: Assessing the eddy covariance technique for evaluating carbon dioxide exchange rates of ecosystems: past, present and future, Glob. Chang. Biol., 9(4), 479–492, 2003.

Beswick, K. M., Gallagher, M. W., Webb, A. R., Norton, E. G. and Perry, F.: Application of the Aventech AIMMS20AQ airborne probe for turbulence measurements during the Convective Storm Initiation Project, Atmos. Chem. Phys., 8(17), 5449–5463, doi:10.5194/acp-8-5449-2008, 2008.

Billesbach, D. P.: Estimating uncertainties in individual eddy covariance flux measurements: a comparison of methods and a proposed new method, Agric. For. Meteorol., 151(3), 394–405, 2011.

Björkegren, A. and Grimmond, C. S. B.: Net carbon dioxide emissions from central London, Urban Clim., 23, 131–158, doi:https://doi.org/10.1016/j.uclim.2016.10.002, 2018.

Brock, F. V: A nonlinear filter to remove impulse noise from meteorological data, J. Atmos. Ocean. Technol., 3(1), 51–58, 1986.

Brookes, D. M., Stedman, J. R., Kent, A. J., King, R. J., Venfield, H. L., Cooke, S. L., Lingard, J. J. N., Vincent, K. J., Bush, T. J. and Abbott, J.: Technical report on UK supplementary assessment under the Air Quality Directive (2008/50/EC), the Air Quality Framework Directive (96/62/EC) and Fourth Daughter Directive (2004/107/EC) for 2011, Rep. Defra UK Devolved Adm., 2013.

Bush, T., Tsagatakis, I., King, K. and Passant, N.: NAEI UK emission mapping methodology 2006., 2008.

Deardorff, J. W.: Three-dimensional numerical study of turbulence in an entraining mixed layer, Boundary-Layer Meteorol., 7(2), 199–226, 1974.

Drew, D. R., Barlow, J. F. and Lane, S. E.: Observations of wind speed profiles over Greater London, UK, using a Doppler lidar, J. Wind Eng. Ind. Aerodyn., 121, 98–105, doi:10.1016/j.jweia.2013.07.019, 2013.

Drummond, J. W., Volz, A. and Ehhalt, D. H.: An optimized chemiluminescence detector for tropospheric NO measurements, J. Atmos. Chem., 2(3), 287–306, 1985.

EEA: EMEP/EEA air pollutant emission inventory guidebook 2013, Eur. Environ. Agency, Copenhagen, 2013.

Elith, J., Leathwick, J. R. and Hastie, T.: A working guide to boosted regression trees, J. Anim. Ecol., doi:10.1111/j.1365-2656.2008.01390.x, 2008.

Esri: "Human Geography Base" [basemap]. Scale Not Given., [online] Available from: https://basemaps.arcgis.com/arcgis/rest/services/World_Basemap_v2/VectorTileServer (Accessed 1 March 2021a), 2021.

Esri: "Human Geography Base" [basemap]. Scale Not Given., 2021b.

Famulari, D., Nemitz, E., Di Marco, C., Phillips, G. J., Thomas, R., House, E. and Fowler, D.: Eddy-covariance measurements of nitrous oxide fluxes above a city, Agric. For. Meteorol., doi:10.1016/j.agrformet.2009.08.003, 2010.

Foken, T. and Wichura, B.: Tools for quality assessment of surface-based flux measurements, Agric. For. Meteorol., doi:10.1016/0168-1923(95)02248-1, 1996.

Font, A., Grimmond, C. S. B., Kotthaus, S., Morguí, J.-A., Stockdale, C., O'Connor, E., Priestman, M. and Barratt, B.: Daytime CO2 urban surface fluxes from airborne measurements, eddy-covariance observations and emissions inventory in Greater London, Environ. Pollut., 196, 98–106, doi:https://doi.org/10.1016/j.envpol.2014.10.001, 2015.

Foster, W. M., Brown, R. H., Macri, K. and Mitchell, C. S.: Bronchial reactivity of healthy subjects: 18–20 h postexposure to ozone, J. Appl. Physiol., 89(5), 1804–1810, 2000.

Grange, S. K., Lewis, A. C., Moller, S. J. and Carslaw, D. C.: Lower vehicular primary emissions of NO2 in Europe than assumed in policy projections, Nat. Geosci., 10(12), 914, 2017.

Greater London Authority: London Atmospheric Emissions Inventory (LAEI) 2013, [online] Available from: https://data.london.gov.uk/dataset/london-atmospheric-emissions-inventory-2013, 2013.

Hartmann, J., Gehrmann, M., Kohnert, K., Metzger, S. and Sachs, T.: New calibration procedures for airborne turbulence measurements and accuracy of the methane fluxes during the AirMeth campaigns, Atmos. Meas. Tech., 11(7), 4567–4581, doi:10.5194/amt-11-4567-2018, 2018.

Hastie, T. J. and Tibshirani, R. J.: Generalized additive models, CRC press., 1990.

Hersbach, H., Bell, B., Berrisford, P., Biavati, G., Horányi, A., Muñoz Sabater, J., Nicolas, J., Peubey, C., Radu, R., Rozum, I., Schepers, D., Simmons, A., Soci, C., Dee, D. and Thépaut, J.-N.: ERA5 hourly data on single levels from 1979 to present., Copernicus Clim. Chang. Serv. Clim. Data Store, doi:10.24381/cds.adbb2d47, 2018.

Ingle, J. D. and Crouch, S. R.: Critical comparison of photon counting and direct current measurement techniques for quantitative spectrometric methods, Anal. Chem., 44(4), 785–794, 1972.

Karl, T., Guenther, A., Lindinger, C., Jordan, A., Fall, R. and Lindinger, W.: Eddy covariance measurements of oxygenated volatile organic compound fluxes from crop harvesting using a redesigned proton-transfer-reaction mass spectrometer, J. Geophys. Res., 106(D20), 24157–24167, doi:10.1029/2000jd000112, 2001.

Karl, T., Misztal, P. K., Jonsson, H. H., Shertz, S., Goldstein, A. H. and Guenther, A. B.: Airborne Flux Measurements of BVOCs above Californian Oak Forests: Experimental Investigation of Surface and Entrainment Fluxes, OH Densities, and Damkohler Numbers, J. Atmos. Sci., 70(10), 3277–3287, doi:Doi 10.1175/Jas-D-13-054.1, 2013.

Karl, T., Graus, M., Striednig, M., Lamprecht, C., Hammerle, A., Wohlfahrt, G., Held, A., Von Der Heyden, L., Deventer, M. J., Krismer, A., Haun, C., Feichter, R. and Lee, J.: Urban eddy covariance measurements reveal significant missing NO x emissions in Central Europe, Sci. Rep., doi:10.1038/s41598-017-02699-9, 2017.

Karl, T. G., Spirig, C., Rinne, J., Stroud, C., Prevost, P., Greenberg, J., Fall, R. and Guenther, A.: Virtual disjunct eddy covariance measurements of organic compound fluxes from a subalpine forest using proton transfer reaction mass spectrometry, Atmos. Chem. Phys., 2(4), 279–291, 2002.

Kelly, F. J. and Fussell, J. C.: Role of oxidative stress in cardiovascular disease outcomes following exposure to ambient air pollution, Free Radic. Biol. Med., 110, 345–367, 2017.

Kley, D. and McFarland, M.: Chemiluminescence detector for NO and NO2, Atmos. Technol.;(United States), 12, 1980.

Kljun, N., Rotach, M. W. and Schmid, H. P.: A three-dimensional backward lagrangian footprint model for a wide range of boundary-layer stratifications, Boundary-Layer Meteorol., 103(2), 205–226, doi:Doi 10.1023/A:1014556300021, 2002.

Kljun, N., Calanca, P., Rotach, M. W. and Schmid, H. P.: A simple parameterisation for flux footprint predictions, Boundary-Layer Meteorol., 112(3), 503–523, doi:Doi 10.1023/B:Boun.0000030653.71031.96, 2004.

Lang, P. E., Carslaw, D. C. and Moller, S. J.: A trend analysis approach for air quality network data, Atmos. Environ. X, 100030, 2019.

Langford, B., Davison, B., Nemitz, E. and Hewitt, C. N.: Mixing ratios and eddy covariance flux measurements of volatile organic compounds from an urban canopy (Manchester, UK), Atmos. Chem. Phys., 9(6), 1971–1987, 2009.

Langford, B., Nemitz, E., House, E., Phillips, G. J., Famulari, D., Davison, B., Hopkins, J. R., Lewis, A. C. and Hewitt, C. N.: Fluxes and concentrations of volatile organic compounds above central London, UK, Atmos. Chem. Phys., 10(2), 627–645, doi:10.5194/acp-10-627-2010, 2010.

Lee, J. D., Moller, S. J., Read, K. A., Lewis, A. C., Mendes, L. and Carpenter, L. J.: Year-round measurements of nitrogen oxides and ozone in the tropical North Atlantic marine boundary layer, J. Geophys. Res., 114, doi:Artn D21302 10.1029/2009jd011878, 2009.

Lee, J. D., Helfter, C., Purvis, R. M., Beevers, S. D., Carslaw, D. C., Lewis, A. C., Moller, S. J., Tremper, A., Vaughan, A. and Nemitz, E. G.: Measurement of NOx Fluxes from a Tall Tower in Central London, UK and Comparison with Emissions Inventories, Environ. Sci. Technol., 49(2), 1025–1034, doi:10.1021/es5049072, 2015.

Lenschow, D. H., Mann, J. and Kristensen, L.: How long is long enough when measuring fluxes and other turbulence statistics?, J. Atmos. Ocean. Technol., 11(3), 661–673, 1994.

Mann, J. and Lenschow, D. H.: Errors in Airborne Flux Measurements, J. Geophys. Res., 99(D7), 14519–14526, doi:Doi 10.1029/94jd00737, 1994.

Marr, L. C., Moore, T. O., Klapmeyer, M. E. and Killar, M. B.: Comparison of NOx fluxes measured by eddy covariance to emission inventories and land use, Environ. Sci. Technol., doi:10.1021/es303150y, 2013.

Metzger, S.: Surface-atmosphere exchange in a box: Making the control volume a suitable representation for in-situ observations, Agric. For. Meteorol., doi:10.1016/j.agrformet.2017.08.037, 2018.

Metzger, S., Junkermann, W., Mauder, M., Beyrich, F., Butterbach-Bahl, K., Schmid, H. P. and Foken, T.: Eddy-covariance flux measurements with a weight-shift microlight aircraft, Atmos. Meas. Tech., 5(7), 1699–1717, doi:10.5194/amt-5-1699-2012, 2012.

Metzger, S., Junkermann, W., Mauder, M., Butterbach-Bahl, K., Widemann, B. T. Y., Neidl, F., Schafer, K., Wieneke, S., Zheng, X. H., Schmid, H. P. and Foken, T.: Spatially explicit regionalization of airborne flux measurements using environmental response functions, Biogeosciences, 10(4), 2193–2217, doi:DOI 10.5194/bg-10-2193-2013, 2013.

Metzger, S., Durden, D., Sturtevant, C., Luo, H., Pingintha-Durden, N., Sachs, T., Serafimovich, A., Hartmann, J., Li, J. and Xu, K.: eddy4R 0.2. 0: a DevOps model for community-extensible processing and analysis of eddy-covariance data based on

R, Git, Docker, and HDF5, Geosci. Model Dev., 10(9), 3189, 2017.

Misztal, P. K., Karl, T., Weber, R., Jonsson, H. H., Guenther, A. B. and Goldstein, A. H.: Airborne flux measurements of biogenic isoprene over California, Atmos. Chem. Phys., 14(19), 10631–10647, doi:DOI 10.5194/acp-14-10631-2014, 2014.

Mudway, I. S., Dundas, I., Wood, H. E., Marlin, N., Jamaludin, J. B., Bremner, S. A., Cross, L., Grieve, A., Nanzer, A. and Barratt, B. M.: Impact of London's low emission zone on air quality and children's respiratory health: a sequential annual cross-sectional study, Lancet Public Heal., 4(1), e28--e40, 2019.

Nordbo, A. and Katul, G.: A Wavelet-Based Correction Method for Eddy-Covariance High-Frequency Losses in Scalar Concentration Measurements, Boundary-Layer Meteorol., 146(1), 81–102, doi:10.1007/s10546-012-9759-9, 2013.

OpenStreetMap contributors: Planet dump retrieved from https://planet.osm.org, [online] Available from: https://www.openstreetmap.org, 2021.

Ordnance Survey: Simple Building Heights, [online] Available from: https://digimap.edina.ac.uk/, 2020.

Padgham, M., Rudis, B., Lovelace, R., Salmon, M., Smith, A., Smith, J., Gilardi, A., Spinielli, E., Kalicinski, M., Noam, F. and Lukasz, B.: osmdata: Import "OpenStreetMap" Data as Simple Features or Spatial Objects, R Packag. version 0.1.4 [online] Available from: https://cran.r-project.org/web/packages/osmdata/index.html, 2020.

Pitt, J. R., Allen, G., Bauguitte, S. J. B., Gallagher, M. W., Lee, J. D., Drysdale, W., Nelson, B., Manning, A. J. and Palmer, P. I.: Assessing London CO2, CH4 and CO emissions using aircraft measurements and dispersion modelling, Atmos. Chem. Phys., doi:10.5194/acp-19-8931-2019, 2019.

Reed, C., Evans, M. J., Carlo, P. D., Lee, J. D. and Carpenter, L. J.: Interferences in photolytic NO2 measurements: explanation for an apparent missing oxidant?, Atmos. Chem. Phys., 16(7), 4707–4724, 2016.

Serafimovich, A., Metzger, S., Hartmann, J., Kohnert, K., Zona, D. and Sachs, T.: Upscaling surface energy fluxes over the North Slope of Alaska using airborne eddy-covariance measurements and environmental response functions, Atmos. Chem. Phys., doi:10.5194/acp-18-10007-2018, 2018.

Shao, J., Zosky, G. R., Hall, G. L., Wheeler, A. J., Dharmage, S., Foong, R., Knibbs, L. and Johnston, F. H.: Ambient Nitrogen Dioxide Exposure During Infancy Influences Respiratory Mechanics in Preschool Years, in D96. ENVIRONMENTAL ASTHMA EPIDEMIOLOGY, pp. A7058--A7058, American Thoracic Society., 2019.

Shaw, M. D., Lee, J. D., Davison, B., Vaughan, A., Purvis, R. M., Harvey, A., Lewis, A. C. and Hewitt, C. N.: Airborne determination of the temporo-spatial distribution of benzene, toluene, nitrogen oxides and ozone in the boundary layer across Greater London, UK, Atmos. Chem. Phys., 15(9), 5083–5097, doi:10.5194/acp-15-5083-2015, 2015.

Silvia, D. and Skilling, J.: Data analysis: a Bayesian tutorial, OUP Oxford., 2006.

Sorbjan, Z.: Statistics of scalar fields in the atmospheric boundary layer based on large-eddy simulations. Part II: Forced convection, Boundary-layer Meteorol., 119(1), 57–79, 2006.

Squires, F. A., Nemitz, E., Langford, B., Wild, O., Drysdale, W. S., Acton, W. J. F., Fu, P., Grimmond, C. S. B., Hamilton, J. F., Hewitt, C. N., Hollaway, M., Kotthaus, S., Lee, J., Metzger, S., Pingintha-Durden, N., Shaw, M., Vaughan, A. R., Wang, X., Wu, R., Zhang, Q. and Zhang, Y.: Measurements of traffic-dominated pollutant emissions in a Chinese megacity, Atmos.

Chem. Phys., 20(14), 8737–8761, doi:10.5194/acp-20-8737-2020, 2020.

Starkenburg, D., Metzger, S., Fochesatto, G. J., Alfieri, J. G., Gens, R., Prakash, A. and Cristóbal, J.: Assessment of despiking methods for turbulence data in micrometeorology, J. Atmos. Ocean. Technol., doi:10.1175/JTECH-D-15-0154.1, 2016.

Thomas, C. and Foken, T.: Flux contribution of coherent structures and its implications for the exchange of energy and matter in a tall spruce canopy, Boundary-Layer Meteorol., 123(2), 317–337, doi:10.1007/s10546-006-9144-7, 2007.

Torrence, C. and Compo, G. P.: A practical guide to wavelet analysis, Bull. Am. Meteorol. Soc., 79(1), 61–78, doi:Doi 10.1175/1520-0477(1998)079<0061:Apgtwa>2.0.Co;2, 1998.

Vaughan, A. R., Lee, J. D., Misztal, P. K., Metzger, S., Shaw, M. D., Lewis, A. C., Purvis, R. M., Carslaw, D. C., Goldstein, A. H. and Hewitt, C. N.: Spatially resolved flux measurements of NOx from London suggest significantly higher emissions than predicted by inventories, Faraday Discuss., 189, 455–472, 2016.

Vaughan, A. R., Lee, J. D., Shaw, M. D., Misztal, P., Metzger, S., Vieno, M., Davison, B., Karl, T., Carpenter, L. J., Lewis, A. C., Purvis, R., Goldstein, A. and Hewitt, C. N.: VOC emission rates over London and South East England obtained by airborne eddy covariance, Faraday Discuss., doi:10.1039/C7FD00002B, 2017.

Vickers, D. and Mahrt, L.: Quality control and flux sampling problems for tower and aircraft data, J. Atmos. Ocean. Technol., doi:10.1175/1520-0426(1997)014<0512:QCAFSP>2.0.CO;2, 1997.

Williamson, J. A., Kendall-Tobias, M. W., Buhl, M. and Seibert, M.: Statistical evaluation of dead time effects and pulse pileup in fast photon counting. Introduction of the sequential model, Anal. Chem., 60(20), 2198–2203, 1988.

Wolfe, G. M., Hanisco, T. F., Arkinson, H. L., Bui, T. P., Crounse, J. D., Dean-Day, J., Goldstein, A., Guenther, A., Hall, S. R. and Huey, G.: Supporting information for Quantifying sources and sinks of reactive gases in the lower atmosphere using airborne flux observations, Geophys. Res. Lett., 42(19), 8231–8240, 2015.

Xu, K., Metzger, S. and Desai, A. R.: Upscaling tower-observed turbulent exchange at fine spatio-temporal resolution using environmental response functions, Agric. For. Meteorol., 232, 10–22, doi:10.1016/j.agrformet.2016.07.019, 2017.

Xu, K., Metzger, S. and Desai, A. R.: Surface-atmosphere exchange in a box: Space-time resolved storage and net vertical fluxes from tower-based eddy covariance, Agric. For. Meteorol., 255, 81–91, doi:10.1016/j.agrformet.2017.10.011, 2018.

Yuan, B., Kaser, L., Karl, T., Graus, M., Peischl, J., Campos, T. L., Shertz, S., Apel, E. C., Hornbrook, R. S., Hills, A., Gilman, J. B., Lerner, B. M., Warneke, C., Flocke, F. M., Ryerson, T. B., Guenther, A. B. and de Gouw, J. A.: Airborne flux measurements of methane and volatile organic compounds over the Haynesville and Marcellus shale gas production regions, J. Geophys. Res., 120(12), 6271–6289, doi:10.1002/2015jd023242, 2015.

Zeileis, A. and Grothendieck, G.: Zoo: S3 infrastructure for regular and irregular time series, J. Stat. Softw., doi:10.18637/jss.v014.i06, 2005.

Deleted: Aubinet, M., Vesala, T. and Papale, D.: Eddy covariance: a practical guide to measurement and data analysis, Springer Science & Business Media., 2012.¶
Baldocchi, D. D.: Assessing the eddy covariance technique for evaluating carbon dioxide exchange rates of ecosystems: past, present and future, Glob. Chang. Biol., 9(4), 479–492, 2003.¶
Beswick, K. M., Gallagher, M. W., Webb, A. R., Norton, E. G. and Perry, F.: Application of the Aventech AIMMS20AQ airborne probe for turbulence measurements during the Convective Storm Initiation Project, Atmos. Chem. Phys., 8(17), 5449–5463, doi:10.5194/acp-8-5449-2008, 2008.¶
Billesbach, D. P.: Estimating uncertainties in individual eddy covariance flux measurements: a comparison of methods and a proposed new method, Agric. For. Meteorol., 151(3), 394–405, 2011.¶
Björkegren, A. and Grimmond, C. S. B.: Net carbon dioxide emissions from central London, Urban Clim., 23, 131–158, doi:https://doi.org/10.1016/j.uclim.2016.10.002, 2018.¶
Brock, F. V: A nonlinear filter to remove impulse noise from meteorological data, J. Atmos. Ocean. Technol., 3(1), 51–58, 1986.¶
Brookes, D. M., Stedman, J. R., Kent, A. J., King, R. J., Venfield, H. L., Cooke, S. L., Lingard, J. J. N., Vincent, K. J., Bush, T. J. and Abbott, J.: Technical report on UK supplementary assessment under the Air Quality Directive (2008/50/EC), the Air Quality Framework Directive (96/62/EC) and Fourth Daughter Directive (2004/107/EC) for 2011, Rep. Defra UK Devolved Adm., 2013.¶
Bush, T., Tsagatakis, I., King, K. and Passant, N.: NAEI UK emission mapping methodology 2006., 2008.¶
Core Team, R.: R: A language and environment for statistical computing, R Found. Stat. Comput. Vienna, 2019.¶
Deardorff, J. W.: Three-dimensional numerical study of turbulence in an entraining mixed layer, Boundary-Layer Meteorol., 7(2), 199–226, 1974.¶
Drew, D. R., Barlow, J. F. and Lane, S. E.: Observations of wind speed profiles over Greater London, UK, using a Doppler lidar, J. Wind Eng. Ind. Aerodyn., 121, 98–105, doi:10.1016/j.jweia.2013.07.019, 2013.¶
Drummond, J. W., Volz, A. and Ehhalt, D. H.: An optimized chemiluminescence detector for tropospheric NO measurements, J. Atmos. Chem., 2(3), 287–306, 1985.¶
EEA: EMEP/EEA air pollutant emission inventory guidebook 2013, Eur. Environ. Agency, Copenhagen, 2013.¶
Elith, J., Leathwick, J. R. and Hastie, T.: A working guide to boosted regression trees, J. Anim. Ecol., doi:10.1111/j.1365-2656.2008.01390.x, 2008.¶
Esri: "Human Geography Base" [basemap]. Scale Not Given., [online] Available from: https://basemaps.arcgis.com/arcgis/rest/services/World_Basemap_v2/VectorTileServer (Accessed 1 March 2021a), 2021.¶
Esri: "Human Geography Base" [basemap]. Scale Not Given., 2021b.¶
Famulari, D., Nemitz, E., Di Marco, C., Phillips, G. J., Thomas, R., House, E. and Fowler, D.: Eddy-covariance measurements of nitrous oxide fluxes above a city, Agric. For. Meteorol., doi:10.1016/j.agrformet.2009.08.003, 2010.¶
Foken, T. and Wichura, B.: Tools for quality assessment of surface-based flux measurements, Agric. For. Meteorol., doi:10.1016/0168-1923(95)02248-1, 1996.¶
Font, A., Grimmond, C. S. B., Kotthaus, S., Morguí, J.-A., Stockdale, C., O'Connor, E., Priestman, M. and Barratt, B.: Daytime CO2 urban surface fluxes from airborne measurements, eddy-covariance observations and emissions inventory in Greater London, Environ. Pollut., 196, 98–106, doi:https://doi.org/10.1016/j.envpol.2014.10.001, 2015.¶
Foster, W. M., Brown, R. H., Macri, K. and Mitchell, C. S.: ... [9]